Experimental and Analytical Study of Countercurrent Flow Limitation in Vertical Gas/Liquid Flows

Martin Stephan and Franz Mayinger*

An experimental and analytical study of adiabatic countercurrent flow limitation (flooding) in single vertical ducts is reported. The experiments were carried out in a rectangular channel using saturated liquid and vapour of Refrigerant 12 (CCl_2F_2). The steady-state liquid delivery (flooding) curves as well as local pressure drop and void fraction distributions in the countercurrent flow were measured in a range of system pressures from $p/p_{crit} = 0.16$ to $p/p_{crit} = 0.31$, and for various total liquid injection rates and locations. The measured flooding curves $j_l = f(j_g)$ as well as pressure drop and void fraction during partial liquid delivery ($j_l < j_l^{in}$) were not affected either by the axial liquid feed location or by the excess liquid rate carried upwards by the vapour. Moreover, for given flow conditions during flooding pressure drop and void fraction were essentially the same at different axial positions. Radial void fraction distributions evaluated from optical fibre probe data indicate an annular-type flow pattern. Based on this experimental evidence, a mechanistic core/film flow model was developed for the calculation of flooding. The analytical results are compared with the present high pressure and with comparable atmospheric pressure experimental data, showing reasonable overall predictions not only of the flooding curves, but also of the pressure drop in countercurrent flow.

1 Introduction

In vertical two-phase flow, the process of flooding leads to the limitation of the liquid downflow penetrating through a given gas or vapour upflow. The flooding phenomenon is important for the prediction of decay heat removal after hypothetical loss-of-coolant accidents in nuclear reactors and, particularly, for a variety of applications in the chemical industry, such as the design of reflux condensers or packed columns. Flooding has been the subject of numerous experimental and some analytical studies over the past few decades. The experimental work focussed mainly on adiabatic flooding in single channels, but also on the effects of multiple-path geometries or of interfacial condensation in the case of subcooled liquid injection. Analytical models may be classified into three categories according to whether they are based on entrainment, wave instability or film flow mechanisms. Extensive reviews of this work have been published by Bankoff and Lee [1] and by Tien and Liu [2].

Due to the complexity of the problem, the most widely used tools to predict flooding are essentially empirically derived equations, such as correlations of Wallis [3], Pushkina and Sorokin [4], Feind [5] and Alekseev et al. [6, 7]. These correlations yield accurate results only for experimental conditions similar to those, for which they had been developed since the combined effects of crucial parameters, such as channel dimensions and fluid properties are not always accounted for in detail. In addition, even in the relatively simple case of countercurrent flow in vertical single channels, the physical interpretations of the phenomenon have been rather ambiguous in the various investigations. The applied flooding criteria are not always explicitly explained and cover a wide range of flow conditions, from entrainment of droplets to complete reversal of the liquid flow. Such discrepancies may have significantly contributed to the observed spread between various experimental flooding results.

As a step towards a consistent prediction of flooding, the main purpose of this work is to contribute to the understanding and modelling of the flooding phenomenon in single channels under well-defined conditions. The countercurrent flow is investigated experimentally during steady-state operation and under flow conditions where only part of the injected liquid penetrates downwards, the remainder being carried upwards by the vapour flow ("partial liquid delivery"). Under these conditions, which are illustrated schematically in Fig. 1, the countercurrent flow rates below the liquid inlet, expressed here as superficial velocities j_l and j_g, definitively represent the maximum flow rates possible under steady-state conditions.

Therefore, the countercurrent flow limitation can be investigated more consistently with such an experimental concept than by applying other flooding criteria, which may be ambiguous or involve hysteresis effects [8].

For the derivation of a physically consistent flooding model, more information is required on the predominant mechanisms of countercurrent flow limitation and on the flow pattern during flooding. In this study, the pressure drop at various locations as well as local distributions of the void fraction are measured, in order to provide such information on the flooding process.

At present, little is known about the influence of system pressure on flooding. In particular, there is some doubt as to whether the well-known empirical correlations [3 – 7] based on

* Dr.-Ing. M. Stephan and Prof. Dr.-Ing. F. Mayinger, Lehrstuhl A für Thermodynamik, Technische Universität München, Arcisstr. 21, D-8000 München 2.

0930-7516/92/0102-0051 $03.50+.25/0

Chem. Eng. Technol. 15 (1992) 51 – 62

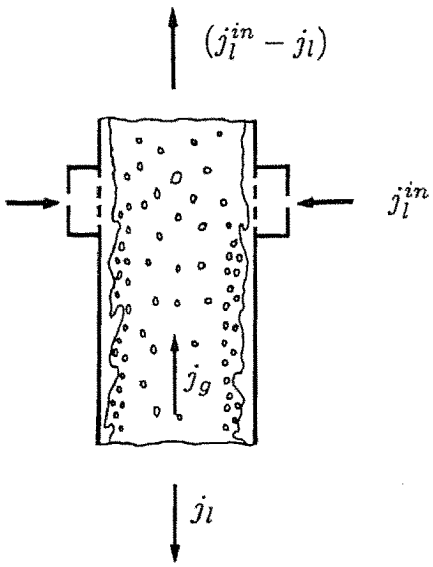

Fig. 1. Flow distribution during "partial liquid delivery" (flooding).

atmospheric pressure experiments can be extrapolated to high reduced pressures, i.e. high gas-phase densities, which are of importance in various applications. In the present experiments, Refrigerant 12 is used as the model fluid, in order to enlarge the data basis in this pressure range and to investigate the effect of system pressure on flooding. Using R 12, changes in pressure affect not only gas-phase and liquid densities but also other crucial properties such as surface tension and liquid viscosity. The experimental results obtained in this work may thus contribute to the classification of the effects of individual parameters on flooding and to the assessment of the analytical flooding model presented in this paper.

2 Experimental Set-up

The experiments were carried out using a closed test loop, which is shown schematically in Fig. 2.

The rectangular test section is installed in a cylindrical pressure vessel about 3 m in height (bold faced outline in the figure). The test section inlet and outlet vapour flow rates are measured using vortex shedding flowmeters while turbine flowmeters are used to measure the liquid injection rate as well as the net liquid downflow and excess upflow rates. Fig. 3 shows a diagram of the test section, including the optical probe set-up for local void fraction measurements.

The liquid is injected as a falling film via porous sintered plates mounted flush with one of the larger channel walls, at two axial levels, either of which may be used. Viewing windows are installed at the two smaller sides for flow observation. Pressure gradients were measured at four axial positions, in the countercurrent and cocurrent flow regions, using capacitance differential pressure transducers. The distance between two successive pressure taps is 0.3 m.

Miniaturized optical fibre probes are installed at two axial levels, to measure the local void or liquid fraction during

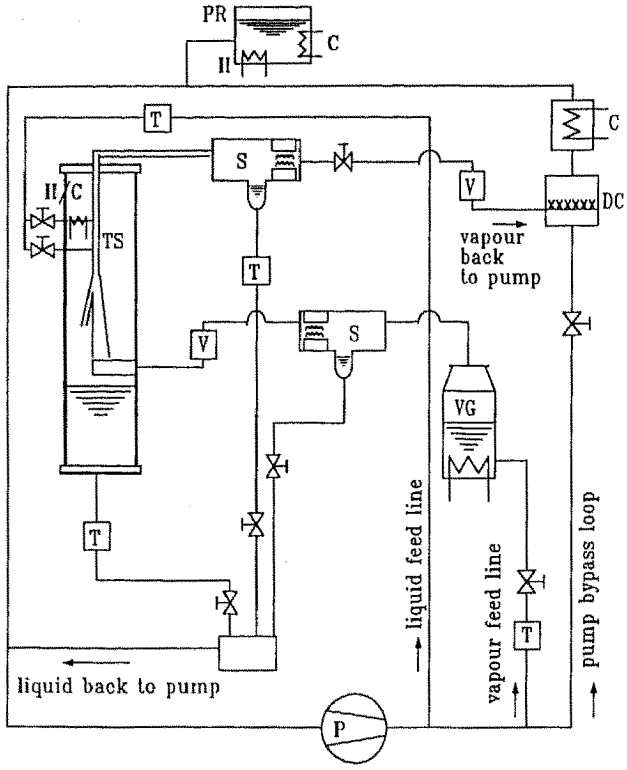

Fig. 2. Schematic diagram of test loop.

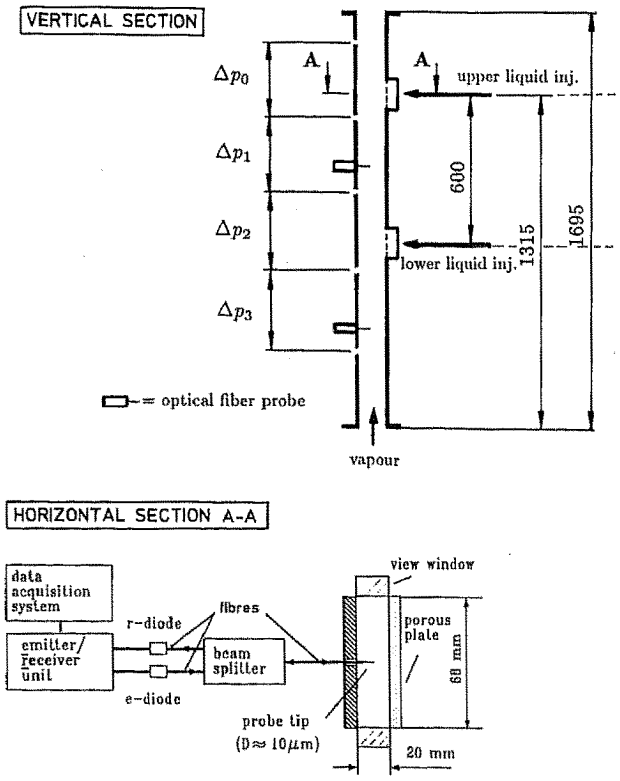

Fig. 3. Test section and optical fibre probe set-up.

flooding. The probes are adjustable horizontally by means of micrometer gauges. Depending on the different refractive indices of the phases in contact with the probe tip at a given moment (vapour or liquid), either a very large or a very small part of the emitted light is reflected at the tip, transmitted via a beam splitter to a receiver diode and, subsequently, transformed into an analog output signal. The local liquid fraction values were evaluated from the time traces of these signals according to a method, which is outlined in the following. The probe arrangement, used in this study, was developed by Auracher and Marroquin [9] and provides a very high vapour-to-liquid signal amplitude, i.e. of the order of 10 V. The extremely small probe tip ($D \approx 10$ μm) allows detection of very small droplets.

3 Test Conditions and Procedure

In this paper, results are presented of selected test series at three different system pressures. An overview of the essential properties of saturated Refrigerant 12 at these pressures is given in Table 1.

Table 1. Properties of saturated R 12 for selected test series.

		Test series No.		
		I	II	III
System pressure p	[MPa]	0.67	1.0	1.3
Critical pressure ratio p/p_{crit}	[−]	0.16	0.24	0.31
Saturation temperature T_S	[°C]	26	41.5	52.5
Liquid density ϱ_l	[kg/m^3]	1305	1245	1198
Vapour density ϱ_g	[kg/m^3]	38.0	57.1	74.9
Phase density ratio ϱ_l/ϱ_g	[−]	34.3	21.8	16.0
Surface tension σ	[10^3 N/m]	8.6	6.7	5.2
Liquid viscosity η_l	[10^6 kg/ms]	210	180	150

All test series included runs with different total liquid injection rates. In test series I and II, the location of liquid injection was varied. The temperatures of the injected liquid and vapour were always equal to the saturation temperature (adiabatic conditions). For practical reasons, the test runs were generally performed by setting a fixed vapour flow rate and then adjusting the liquid injection rate to its desired value. This test procedure did not produce any ambiguity in the results since neither the different ways of approach to flooding, such as fixing the liquid flow rate first and then adjusting the vapour flow rate, or vice versa, nor a very slow or stepwise approach to flooding conditions, affected the flow conditions or the limiting countercurrent flow rates under steady-state conditions.

4 Test Results and Discussion

4.1 Flooding Curves

Fig. 4 shows, in terms of superficial velocities j_i of both phases, the experimental flooding curves $j_l = f(j_g)$ for the selected system pressures as continuous, dash-dot and broken lines, respectively.

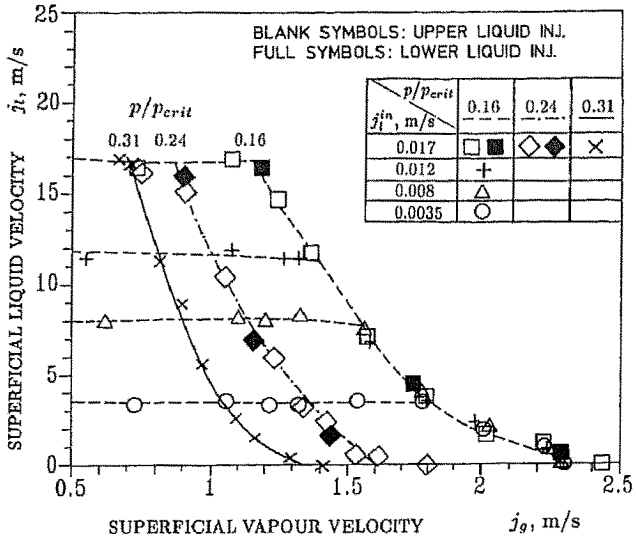

Fig. 4. Measured flooding curves (p = 0.67, 1.0 and 1.3 MPa).

Each flooding curve separates a region to the left of the curve, where steady-state countercurrent flow is possible, from a region to the right of the curve, which is inaccessible under steady-state conditions. The broken horizontal lines refer to $p/p_{crit} = 0.16$ and connect the "stable" operating points, where the total liquid flow is directed downwards, at constant liquid injection rates (j_l^{in} = const).

As a consequence of high upflow momentum caused by high vapour densities, the gas-phase velocities necessary to produce flooding are almost one order of magnitude lower than those in atmospheric pressure tests, reported in the literature. For the same reason, the flooding curves, shown in Fig. 4, become displaced to lower vapour velocities with increasing system pressure.

In agreement with previously reported results of Kröning [10], Celata et al. [11], Zabaras and Dukler [12, 13] and other investigators, the present data reveal essentially no effect of the total liquid injection rate on flooding curves, i.e. on maximum possible downflow rates. In the investigated flow rate range, this result was obtained irrespective of the system pressure and is shown in Fig. 4 for $p/p_{crit} = 0.16$. This means that, in our tests, the flooding process was obviously not affected by excess liquid flow carried upwards by the gas phase. However, Krönning [10] found that the flooding curves were displaced to lower gas velocities with increasing total flow rate of the injected liquid, when using a weir instead of porous plate feed. Celata et al. [11] reported the same trend for the highest liquid injection rate applied in their tests. These results suggest that excessive liquid entrainment and carry-over near the liquid feed location may reduce liquid downflow rates in the case of high liquid injection rates and/or unsuitable injection devices. Experimental flooding curves, obtained in the presence of such secondary effects, are clearly not comparable to the present data, where no effect due to liquid injection rate was observed. The latter finding indicates that the liquid downflow rate is unambiguously controlled by a flow limiting process within the channel rather than by any particular entrance conditions.

As shown in Fig. 4, changes in the length of the countercurrent flow region made by using different liquid injection locations, did not affect the measured liquid delivery (flooding) curves in our tests. Previously, the effects of the length of this region on flooding have frequently been observed in investigations, where sudden flow pattern changes during a continuous increase in the gas-phase flow rate were chosen as the relevant criterion for flooding (Hewitt et al. [14], McQuillan et al. [15], Suzuki and Ueda [16]). Observations made by these investigators indicate that, in this particular mode of operation, the effects of channel length are related to the increase of liquid film waviness with the distance from the inlet, causing a disturbed or chaotic flow pattern to occur at lower gas velocities in longer channels. However, our results as well as the data of Zabaras and Dukler [12] provide some evidence that the length of the countercurrent flow region does not affect the steady-state liquid delivery process, as it is considered in this study. More detailed information on the physical background of particular effects, which may or may not be observed, depending on the applied definition of flooding, is given in [8].

4.2 *Pressure Drop*

Fig. 5 shows examples of measured pressure gradients in the countercurrent flow region below the liquid injection plate, for a system pressure of 0.67 MPa. Similar trends are obtained at other pressures. The accuracy of the presented data is of the order of ± 50 Pa/m.

In "stable" countercurrent flow, i.e. at vapour velocities considerably lower than those needed for flooding, both frictional pressure drop and entrained liquid fraction are obviously negligible compared to the hydrostatic pressure drop of the gas phase only ($\Rightarrow$ $dp/dz \approx (dp/dz)_g^{hydrostat}$). With increasing vapour flow rate and at constant total liquid injection rates, the pressure drop increases in a range of vapour velocities close to the point of first net liquid upflow ("onset of flooding") and then shows a decreasing tendency up to the total liquid carry-over point ($j_l = 0$). This latter trend during flooding reflects the decreasing interfacial momentum transfer and/or entrained liquid fraction which results from the gradually reducing liquid downflow rate at increasing vapour upflow rate (see Fig. 4).

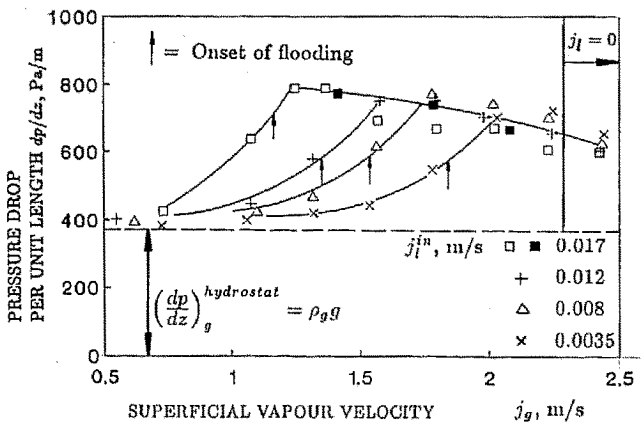

Fig. 5. Measured pressure drop in countercurrent flow region (p = 0.67 MPa; full symbols: measurement position Δp_3, lower liquid injection; blank symbols: measurement position Δp_1, upper liquid injection).

As seen from Fig. 5, the decreasing pressure drop curve during partial liquid delivery (flooding) is essentially independent of the total liquid injection rate, i.e. of the excess liquid rate carried upwards, as well as of the liquid injection level, i.e. the length of the countercurrent flow region. Apparently, these parameters do not significantly affect the flow pattern during flooding, as has already been concluded from Fig. 4 with respect to the actual limiting flooding curves. The pressure drop data thus confirm the above conclusion that the countercurrent flow limiting process appears to be controlled by hydrodynamic phenomena within the channel, and not at the liquid inlet, outlet or other particular locations.

The pressure drop data, presented in Fig. 5, refer to the particular section just below the liquid injection plate (for identification of measurement positions, compare Fig. 3). Taking into account the mentioned accuracy range, additional pressure drop data obtained at other measurement positions in the countercurrent flow region are essentially identical to those shown in Fig. 5 [8]. Physically, this is in agreement with the observation that variations in the length of the countercurrent flow region neither alter the liquid delivery curves (Fig. 4) nor affect the pressure drop during flooding (Fig. 5), and may be explained by the particular flow conditions in the case of flooding. Since, in this case, both phases flow in countercurrent at their maximum possible rates, the entrainment and de-entrainment of droplets at the vapour/liquid interface is likely to produce a very intense interfacial momentum transfer, thus suppressing entrance effects. In contrast to cocurrent annular flow, the state of hydrodynamic equilibrium (∂ (...)/∂z = 0) may therefore be reached after very short lengths, during flooding in countercurrent flow.

As shown in Fig. 5, the pressure drop curve near the onset of flooding is relatively flat at constant liquid injection rates, and covers a wide range of vapour velocities. This is in close agreement with recent rectangular channel data of Biage [17], but in contrast to results of Zabaras [13] from circular tube tests, where the Δp-increase was steeper and did not continue beyond the onset of flooding. Based on our visual observations, this difference in the pressure drop characteristics is related to the fact that, in the present tests, only one wall was wetted by a liquid film prior to flooding, in contrast to circular tube experiments. Therefore, a redistribution of the falling liquid film over other channel walls was observed during the development of flooding. As described in more detail in [8], the competing processes of azimuthal liquid redistribution and liquid carry-over may continue to affect the flow conditions after the onset of flooding, i.e. under steady-state partial liquid delivery conditions. Since these competing processes may depend on the total liquid injection rate, the measured pressure drops are found to be affected by this flow rate, with the particular test section configuration used in this investigation. As shown in Fig. 5, such influence of j_l^{in} on the pressure drop was observed not only for vapour velocities close to the onset of flooding but also for considerably higher vapour flow rates during flooding, where a slight tendency towards higher Δp-values at lower liquid injection rates is evident.

However, in contrast to the mentioned effects of j_l^{in} on the pressure gradient, the flooding curve itself (Fig. 4) is clearly independent of the total liquid injection rate. As outlined in detail in [8], the detected pressure drop variations can be attributed mainly to variations of the droplet fraction in the core flow. However, the core droplet fraction does not significantly affect the countercurrent flow limiting condition, according to the concept of the analytical flooding model, derived in section 6.

4.3 Liquid Fraction

The signal characteristics obtained from optical fibre probe measurements generally indicate that entrained droplets were present in the vapour upflow, during steady-state flooding. Fig. 6 shows an example of a typical output signal. The high voltage level signifies the presence of vapour at the probe tip, whereas the low voltage peaks indicate passages of droplets. For each given flow operating point and probe position, the optical probe signals were sampled during a measurement period Δt_{meas} = 18.2 s, at a frequency of 20 kHz. The applied method to evaluate the wetting period Δt_i of each individual droplet, and thus the local time-averaged liquid fraction $(1-\varepsilon)$, was developed according to the process of wetting when droplets are touching the probe tip, and is illustrated in Fig. 6. Once the output signal starts to decrease below the "vapour level", the considered droplet is already present at the probe tip. On the other hand, the point, where the signal starts to rise again with respect to the "vapour level", is definitely the last one that may be regarded as "wet", in view of possible adhesion effects between the droplet and the tip.

For a system pressure of 0.67 MPa, Fig. 7 shows an example of measured radial distributions of time-averaged liquid fractions between the centreline of the channel and the wall, where the liquid film is introduced.

For the lateral probe positions r = 0,5 and 7 mm, the estimated error band of the presented data is of the order of ± 20%, due to a limited practically feasible recording period resulting in

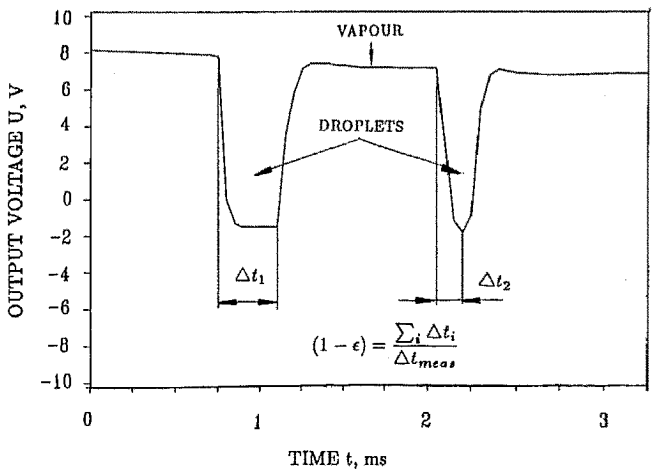

Fig. 6. Typical output signal from an optical fibre probe (p = 0.67 MPa, upper liquid injection, lower probe, centreline position, j_l^{in} = 0.017 m/s, j_g = 1.38 m/s).

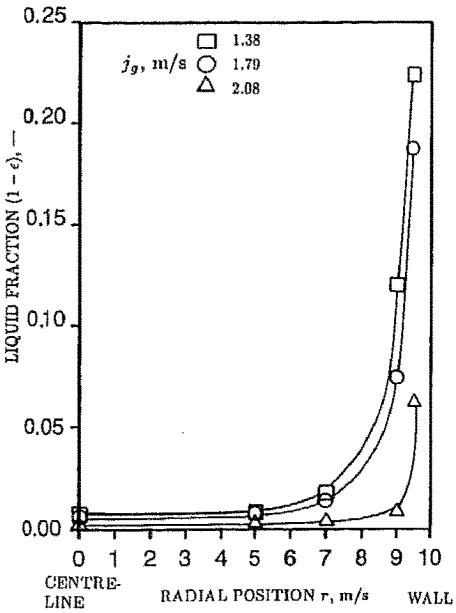

Fig. 7. Measured radial liquid fraction distribution in countercurrent flow region during flooding (p = 0.67 MPa, upper liquid injection, lower probe, j_l^{in} = 0.017 m/s).

non-ideal statistical averaging of the signal, and due to possible systematic errors caused by adhesion effects. For probe positions closer to the wall, the uncertainty range is somewhat wider since the liquid (droplet or film) velocities decrease significantly.

Measured radial liquid fraction distributions in the countercurrent flow region, as presented in Fig. 7, clearly indicate an annular-type flow pattern, with very low liquid fractions over most of the channel width. At each considered position, the liquid fraction decreases with increasing vapour velocity. This is in agreement with the decreasing interfacial wave amplitude established by Zabaras [13] and Emmerechts and Giot [18] from local instantaneous film thickness measurements and with the pressure drop data shown in Fig. 5.

Fig. 8 shows an example of local liquid (droplet) fractions measured at the channel centreline (r = 0 mm), as a function of superficial vapour velocity, for various total liquid injection rates and liquid feed locations. The data refer to a system pressure of 0.67 MPa and to the lower optical probe in the countercurrent flow region.

As expected, the curves are very similar to the pressure drop curves shown in Fig. 5. The above outlined conclusions from the pressure drop data are thus confirmed by the liquid fraction results. This also applies to other investigated system pressures.

The data given in Fig. 8 indicate clearly that even liquid fractions as low as 1% or less can be identified by the optical fibre probes used in this study. In this range of extremely low liquid fractions or high void fractions respectively, suitable reference measurement techniques for the quantitative verification of our

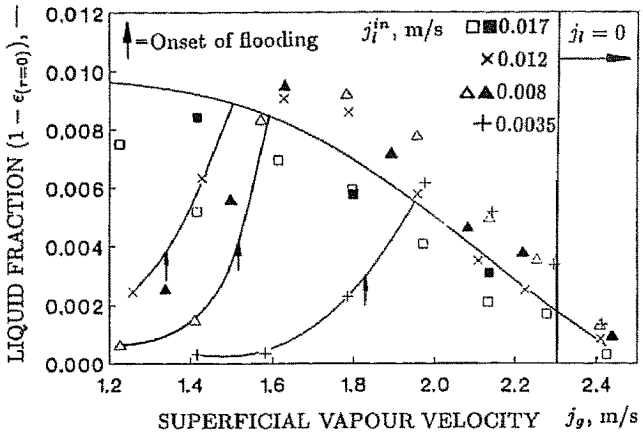

Fig. 8. Measured local liquid fraction at channel centreline in countercurrent flow region (p = 0.67 MPa; full symbols: lower probe, lower liquid injection; blank symbols: upper probe, upper liquid injection).

own results are at present not available [8, 19]. Therefore, the specified uncertainties with respect to the presented data may be considered as acceptable. Moreover, the particularly small optical probes, described in this paper, may be of importance for future measurements of low droplet fractions, in view of the fact that two-phase pressure drops are significantly affected by the presence of even only a few entrained droplets.

The evaluation of droplet sizes or velocities from optical probe data such as those shown in Figs 7 and 8 is doubtful since only wetting periods are measured and no strong correlation between droplet sizes and velocities appears to exist [20, 21]. However, a conservative estimation of maximum droplet sizes is possible by calculating the product of the maximum wetting period within a signal sequence and the local vapour velocity, which is the maximum droplet velocity. For p = 0.67 MPa, and the positions r = 0 mm and r = 5 mm (see Fig. 7), this estimation yields a maximum possible droplet diameter of about 3.5 mm. The actual droplet sizes may be much smaller since, in countercurrent flow, the droplets are likely to travel at considerably lower velocities than the vapour. The presented liquid fraction data thus contradict the concept that a chaotic pattern with liquid bridges across the channel governs the process of flooding in a single channel, as was postulated in a number of analytical studies [22 – 24].

4.4 Phenomenological Conclusions

The essential experimental results presented in the preceding sections may be summarized as follows:

- The flow pattern in "stable" countercurrent flow as well as during steady-state flooding (partial liquid delivery) is annular-mist flow.
- No significant effect of the excess liquid flow rate carried upwards by the vapour or of the length of the countercurrent flow region on the steady-state limiting flooding curves could be established.
- Apart from weak trends associated with particular phenomena caused by the rectangular cross-section and the circumferential location of the liquid injection plates, the pressure drop and core droplet fraction in the countercurrent flow were also found to be independent of the excess liquid rate and of the length of the countercurrent flow region.
- The pressure drop and liquid fraction essentially did not vary along the length of the countercurrent flow region [8].

All these results suggest that the mechanism of countercurrent flow limitation is based on the momentum balance between the two phases along the entire countercurrent flow region, instead of flooding being triggered by local instabilities at the liquid inlet, outlet or other specific locations.

5 Choice of Suitable Reference Experiments

The above phenomenological conclusions drawn from our experimental results constitute the basis of the analytical flooding model, which is formulated in section 6. In order to assess the constitutive conditions within this model, it is necessary to take into account other flooding results from the literature, obtained under comparable experimental conditions. By selecting such reference experiments according to well-defined criteria, it should be guaranteed that the pertinent measured flooding curves would not be significantly affected by secondary fluid dynamic effects or by flooding criteria different from the definition used in this work, and would thus definitively represent the steady-state limiting conditions.

The following criteria are postulated for the choice of reference flooding experiments, comparable to the present ones:

- steady-state experimental conditions in the "partial liquid delivery" range ($j_l < j_l^{in}$),
- liquid downflow rate independent of the total flow rate of injected liquid ($j_l \neq f(j_l^{in})$), at a given gas or vapour upflow rate,
- liquid feed from a large plenum at the upper channel end, and not via a weir.

The exact reasons for applying these particular comparability criteria are described in [8]. These criteria are satisfied by only a small number of published experiments. These selected reference experiments, which were all conducted in circular tubes of various diameters, at near atmospheric pressure and using air for the gas upflow, are listed in Table 2.

Table 2. Test conditions and fluid properties for selected reference experiments ($p \approx p_{atm}$).

	ϱ_l [kg/m³]	ϱ_g [kg/m³]	σ [10³ N/m]	η_l [10⁶ kg/ms]
1 Celata et al. [11], air/water, D = 20 mm	998	1.24	73.5	1150
2 Clift et al. [25], air/glycerol sol., D=31.8 mm	1150	1.24	68.0	10400
3 Zabaras [13], air/water, D = 50.8 mm	998	1.26	73.5	1150
4 Emmerechts and Giot [18], air/water, D = 100 mm	998	1.24	73.5	1150

In the following text, these experiments will be referred to by their numbers 1 to 4, listed in Table 2. In contrast to experiments 1, 3 and 4, which were carried out with water, the liquid used in test 2 was a highly viscous glycerol solution. Moreover, the fluid properties in the low pressure reference experiments listed in Table 2 are very different from those in own high pressure Refrigerant 12 tests (see Table 1). The analytical flooding model, which is described in the next section, may thus be assessed on a relatively broad basis by comparing the calculated and measured results, for the conditions of all the flooding experiments listed in Tables 1 and 2.

6 Analytical Model

6.1 Formulation of the Model

Based on phenomenological conclusions described in section 4.4, a mechanistic core/film flow model was developed to calculate flooding. The model was formulated for circular tubes and is based on the steady-state axial momentum balance equations for a liquid wall film and a gas or vapour core containing droplets. In calculations for non-circular channel cross-sections, such as the rectangular duct used in the present experiments, the hydraulic diameter[1)]

$$D_h = 4\,\frac{A}{P} \tag{1}$$

was substituted for the tube diameter. In Eq. (1), A denotes the total flow area and P the channel perimeter. In view of the fact that, during flooding, the entire perimeter seems to be wetted irrespective of the cross-sectional shape, this approach is physically reasonable, as outlined in detail in [8].

A schematic diagram of the assumed flow pattern, the control volumes underlying the formulation of momentum balance equations and the forces acting on these volumes, is shown in Fig. 9.

The liquid film curvature as well as radial pressure gradients and axial gradients of all variables, except pressure, were neglected. In addition, the acceleration pressure gradient is negligible. A mean film thickness δ and a mean axial velocity $\bar{u}_g$ were assigned to the liquid film and to the gas within the core flow, respectively. The interfacial momentum transfer including all possible contributions, such as shear stress, interfacial wave motion and droplet entrainment and de-entrainment, was modelled by an empirical friction factor f_i relating the total interfacial stress τ_i to the momentum of the gas flow

$$f_i = \frac{\tau_i}{(\varrho_g \bar{u}_g^2)/2} \tag{2}$$

Within the liquid film, velocity profiles were taken into account, in order to avoid the use of a purely empirical wall friction factor. For the calculations of the profiles, the film was

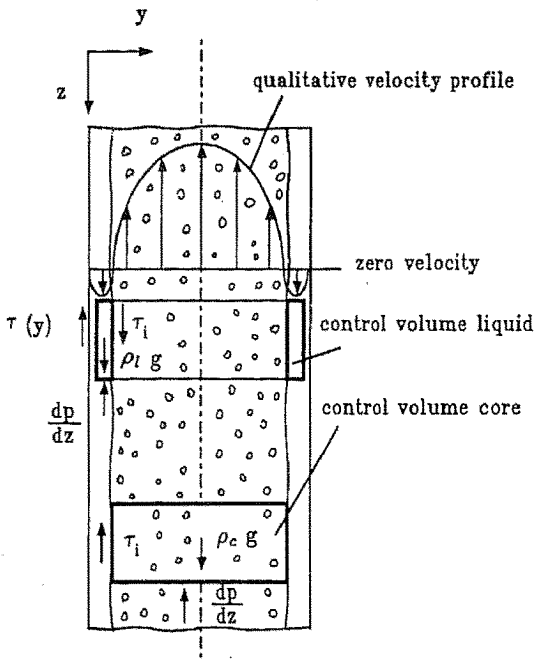

Fig. 9. Core/film flow model.

assumed to be in the laminar flow regime. The local shear stress within the liquid film is then given by

$$\tau(y) = \eta_l \frac{\partial u_l}{\partial y} = \eta_l \frac{\mathrm{d}u_l}{\mathrm{d}y} \tag{3}$$

In our calculations, which covered a range of liquid film Reynolds numbers $\mathrm{Re}_l = \bar{u}_l \delta / \nu_l$ of up to the order of 10^3, experimental pressure drop data could generally be better predicted with the laminar flow assumption than by assuming various degrees of turbulence. This is in agreement with theoretical considerations of Moalem Maron and Dukler [26] suggesting that, in wavy film flow, a considerable part of the liquid is transported within the surface waves. Therefore, the substrate film near the wall, where the relatively high local velocity gradient controls the overall flow conditions, may be laminar even at relatively high Reynolds numbers of the entire film (substrate + waves).

The basic equations underlying the flooding model proposed in this paper are briefly explained in what follows. A detailed description of all the equations and of the calculation procedure is given in [8]. Combining the integral momentum balances over the two control volumes illustrated in Fig. 9 by eliminating the pressure drop between them, yields the local shear stress within the liquid film

$$\bar{\varepsilon}(y) = \tau_i + (\varrho_l - \varrho_c) g\,(\delta - y) \tag{4}$$

where ϱ_c is the average density of the core flow containing droplets

$$\varrho_c = (1 - \bar{\varepsilon}_c)\,\varrho_l + \bar{\varepsilon}_c \varrho_g \tag{5}$$

1) List of symbols at the end of the paper.

with $\bar{\varepsilon}_c$ being the void fraction space-averaged over the core flow area. Eliminating $\tau(y)$ from Eqs (3) and (4), integration of the local velocity gradient and, subsequently, the local velocity over the film thickness yields a relationship of the form

$$\tau_i = f_1(\bar{u}_l, \delta) \quad . \tag{6}$$

Provided that the interfacial friction factor is expressed as a function of $\bar{u}_g$, δ and other known variables (see section 6.2), Eq. (2) represents a relationship of the form

$$\tau_i = f_2(\bar{u}_g, \delta) \quad . \tag{7}$$

Since we have

$$j_g = \bar{u}_g \frac{A_g}{A} = \bar{u}_g \frac{A_c}{A} \bar{\varepsilon}_c = \bar{u}_g \left(1 - \frac{2\delta}{D}\right) \bar{\varepsilon}_c \tag{8}$$

and

$$j_l = \bar{u}_l \frac{A_l}{A} = \bar{u}_l \frac{P}{A} \delta = \bar{u}_l \frac{4\,\delta}{D} \quad , \tag{9}$$

Eqs (6) and (7) may also be written as

$$\tau_i = f_1(j_l, \delta) \tag{6a}$$

and

$$\tau_i = f_2(j_g, \delta) \quad . \tag{7a}$$

Eliminating τ_i from Eqs (6a) and (7a) we obtain a relationship of the form

$$F(j_l, j_g, \delta) = 0 \tag{10}$$

which, up to this point, has been developed from the phase momentum balance equations only. The form of Eq. (10) indicates that the solution of the overall momentum balance requires two variables to be fixed independently (for practical reasons, these variables were taken to be τ_i and δ in our calculations). Therefore, any arbitrary countercurrent flow operating point in the (j_l, j_g)-plane may be generated by solving only the momentum balance equations, and an additional equation is needed to calculate the limiting flooding curves $j_l = f(j_g)$. An interfacial stability analysis, which starts from the assumption of an instantaneous disturbance of the liquid film thickness and was originally developed by Barnea and Taitel [27], yields the equation

$$(\partial\tau_i/\partial\delta)_{j_c = \text{const}} = (\partial\tau_i/\partial\delta)_{j_g = \text{const}} \tag{11}$$

as a limiting condition for the existence of countercurrent flow. Considering Eqs (6a), (7a) and (10), Eq. (11) may be written as

$$\frac{\partial F}{\partial \delta}(j_l, j_g, \delta) = 0 \quad . \tag{12}$$

Combination of Eqs (10) and (12) finally yields the flooding curve

$$j_l = f(j_g) \quad . \tag{13}$$

Mathematically, Eq. (13) represents the envelope of all the solutions of Eq. (10) drawn in the (j_l, j_g)-plane as parameter curves δ = const, thus being equivalent to a flooding solution, which had previously been proposed by a number of investigators but not always with analytical basis [1]. In other words, this envelope represents those solutions of the momentum balance equations, for which maximum values of j_g are obtained at given values of j_l, irrespective of the film thickness. Fig. 10 illustrates an example of a flooding curve calculated in this way.

The j_l = const curves were determined from the above momentum balance equations by an iterative procedure [8]. As a final step, the calculated flooding ("envelope") curve, which is the line connecting the relative maxima of the j_l = const curves, was transformed into a usual (j_l, j_g)-representation (see section 7.1).

It should be borne in mind that the stability criterion introduced by Eq. (12) is quite different from a number of previously reported film stability analyses, which were based on hypothetical assumptions of wave shape, neglected interfacial momentum transfer or assumed liquid bridging to be the dominant mechanism of flooding [22–24]. In contrast to these theories, the present model considers both film stability and interfacial friction, is based on annular flow with no liquid bridging and does not adopt any purely hypothetical assumptions.

6.2 *Core Liquid Fraction*

In order to solve the above model equations, the space-averaged void fraction $\bar{\varepsilon}_c$ in the core flow must be known for the evaluation of Eqs (4) and (8). However, even in the present work, where experimental void fraction data are available, the values of $\bar{\varepsilon}_c$ cannot be evaluated since, using the optical probe measurement technique, it is not possible to accurately deter-

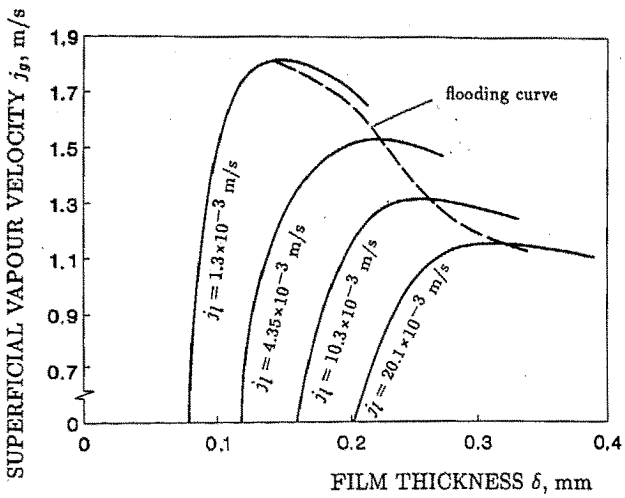

Fig. 10. Example of flooding curve calculated with analytical core/film flow model (conditions of the present R 12 tests for $p = 0.67$ MPa, f_i according to Eq. (18)).

mine the radial position of the core/film interface from liquid fraction distributions such as those shown in Fig. 7 [8]. Therefore, we assume $\bar{\varepsilon}_c = 1$, which is equivalent to $\varrho_c = \varrho_g$. With respect to the calculation of flooding curves, the errors resulting from this simplifying assumption are very small, since $(\varrho_l - \varrho_c) \approx (\varrho_l - \varrho_g)$ and $\bar{\varepsilon}_c \approx 1$ constitute good approximations for the evaluation of Eqs (4) and (8), in the considered range of very high core void fractions ($\bar{\varepsilon}_c > 0.97$).

In contrast to the flooding curve calculations, the difference between ϱ_c and ϱ_g must be accounted for when calculating the pressure drop. According to Eq. (5), in case of the refrigerant flow considered here, this difference may be significant, even for low liquid fractions since the phase density ratio ϱ_l/ϱ_g is relatively low (see Table 1). However, as already explained, the average core density is not known in advance. Therefore, in a first step, the pressure drop was also calculated with the assumption of $\varrho_c = \varrho_g$. From the core momentum balance (see Fig. 9) we then obtain

$$\left(\frac{dp}{dz}\right)_{calc} = \varrho_g\, g - \frac{4\,\tau_i}{D - 2\delta} \tag{14}$$

whereas, due to the presence of droplets in the core flow, the measured pressure drop reads

$$\left(\frac{dp}{dz}\right)_{meas} = \varrho_c\, g - \frac{4\,\tau_i}{D - 2\delta} \tag{15}$$

By introducing Eq. (5) into Eq. (15) and then subtracting Eq. (14) from Eq. (15), we obtain

$$(1 - \bar{\varepsilon}_c) = \frac{(dp/dz)_{meas} - (dp/dz)_{calc}}{(\varrho_l - \varrho_g)\, g} \tag{16}$$

According to Eq. (16), the space-averaged core liquid fraction $(1 - \bar{\varepsilon}_c)$ may be evaluated from comparisons between measured pressure drops and Δp-values calculated under the assumption of ϱ_c equal to ϱ_g. In order to verify the analytical model, these average liquid fraction values can then be roughly checked against estimated values obtained from measured local fraction distributions (see section 7.2).

6.3 *Interfacial Friction Factor*

A physically meaningful correlation for the interfacial factor f_i is necessary for obtaining consistent flooding solutions from the above system of equations. Available empirical equations for cocurrent annular flow, such as the well-known correlation of Wallis [3]

$$f_i = 0.005\,[1 + 300\,(\delta/D] \tag{17}$$

proved to be unsuitable in the case of countercurrent flow, where the interfacial momentum transfer is obviously very intense. Our own and other pressure drop data measured in countercurrent flow are significantly underpredicted by cocurrent flow correlations such as Eq. (17). Therefore, based on assessment calculations using own experimental results and those from the low pressure reference experiments listed in Table 2, a new correlation was developed to describe the interfacial friction in countercurrent flow. This reads

$$f_i = 0.079\ \mathrm{Re}_g^{-0.25}(1 + 115\ \delta^{*N}) \tag{18}$$

where $\mathrm{Re}_g = \bar{u}_g\,(D - 2\delta)/\nu_g$ and $N = 3.95/(1.8 + 3.0/D^*)$. δ^* and D^* are the dimensionless ratios of film thickness and tube diameter, respectively, to the Laplace length $[\sigma/(\varrho_l - \varrho_g)g]^{1/2}$. Eq. (18) constitutes a modification of a correlation proposed by Barathan et al. [28], which is the only published interfacial friction factor correlation for countercurrent flow. For the limiting condition of single-phase flow ($\delta^* = 0$), Eq. (18) is identical to the well-known expression of Blasius, whereas for $\delta^* \neq 0$ the two-phase interfacial friction factor essentially depends on surface tension, liquid viscosity and channel diameter, which is in agreement with experimental trends.

7 Comparison between Analytical and Experimental Results

7.1 *Flooding Curves*

For system pressures of 0.67, 1.0 and 1.3 MPa, Fig. 11 shows calculated and measured flooding curves for the present Refrigerant 12 tests. Fig. 12 presents similar comparisons for the low pressure reference experiments specified in Table 2.

In view of the different hydraulic diameters and fluid properties covered by all these tests, the overall prediction of experimental flooding curves by the present theory is satisfactory. With respect to the comparisons shown in Fig. 11, the reasonable agreement between measured and calculated flooding curves is remarkable since all the relevant fluid properties (ϱ_l, ϱ_g, η_l, σ) change simultaneously, when the system pressure is varied.

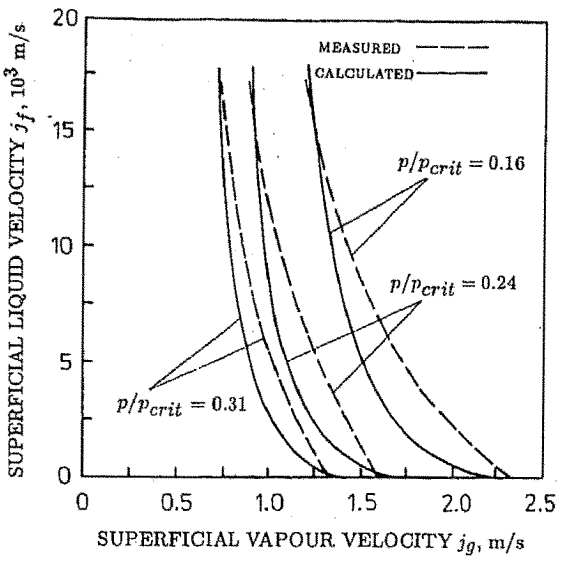

Fig. 11. Measured and analytically calculated flooding curves (conditions of present R 12 tests, f_i according to Eq. (18)).

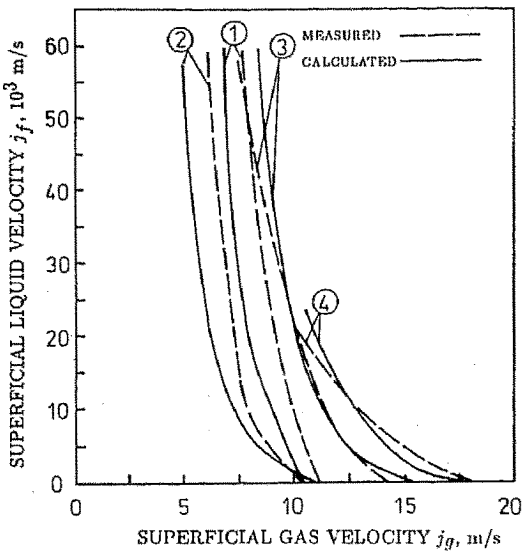

Fig. 12. Measured and analytically calculated flooding curves (conditions of low pressure reference tests 1 to 4, f_i according to Eq. (18)).

Comparing the measured and calculated flooding curves 2 to curves 1 in Fig. 12, it is evident that the highly viscous liquid used in experiment 2 causes the countercurrent flow to "destabilize", i.e. the flooding curve to be displaced to lower gas velocities. Since the film velocity profile is taken into account by the proposed analytical model, this viscosity effect, which is associated with the liquid film being thicker in the case of highly viscous liquids at otherwise comparable conditions, is satisfactorily predicted by the calculations. A comparison between curves 1, 3 and 4 in Fig. 12 indicates that flooding becomes "stabilized" with increasing channel diameter. The reasons for this trend, which is also satisfactorily reflected in the analytical results, are given in [8].

The majority of flooding models proposed in the literature are purely empirical. Among the most widely used are the correlations of Wallis [3], Pushkina and Sorokin [4], Feind [5] and Alekseev et al. [6]. A modified version of the Alekseev equation, proposed by McQuillan and Whalley [7], is of particular interest, since it includes phase densities, tube diameter, surface tension and liquid viscosity, while all the other correlations take only some of the relevant parameters into account. This correlation reads

$$K_g = 0.286\, A^{0.26} B^{-0.22} \left(1 + \frac{\eta_l}{\eta_{water}}\right)^{-0.18} \tag{19}$$

where $K_g = j_g[\varrho_g/[g\sigma(\varrho_l - \varrho_g)]^{1/2}]^{1/2}$ is the Kutateladze number, and A and B are dimensionless constants given by

$$A = \frac{D^2 g(\varrho_l - \varrho_g)}{\sigma} = \left(\frac{D}{\lambda_{crit}}\right)^2 \tag{20}$$

and

$$B = \frac{\dot{V}_l}{P}\left(\frac{g(\varrho_l - \varrho_g)^3}{\sigma^3}\right)^{1/4} \tag{21}$$

In Figs 13 and 14, the flooding curves measured in the present refrigerant tests (Fig. 13) and in the considered low pressure reference experiments (Fig. 14) are compared to the respective curves predicted by Eq. (19).

As seen from the diagrams, all the above described experimental trends are qualitatively reflected in the correlation according to Eq. (19). However, for given superficial liquid velocities, Eq. (19) generally predicts the limiting condition of flooding at superficial gas-phase velocities, which are significantly too low.

It should be noted that the discrepancy between the considered data and flooding predictions from other available empirical correlations [3 – 5] is even more pronounced since not all the crucial parameters are included in these correlations. For example, the frequently used Wallis correlation [3] does not account for the effect of surface tension, whereas the Kutateladze correlation (originally proposed by Puskina and Sorokin [4]) does not reflect the channel diameter and, moreover, neither of these correlations considers the liquid viscosity effect. However, the reducing effect of high gas-phase densities on gas-phase velocities at flooding is satisfactorily predicted by all the mentioned empirical flooding correlations. Therefore, these correlations are suitable at least for approximate estimations of the limiting flooding flow rates in a wide range of system pressures. Summing up, we may conclude that the present analytical flooding model allows the calculation of the steady-state flooding conditions, as they are defined in this work, more precisely than purely empirical correlations.

7.2 Pressure Drop and Liquid Fraction

In addition to calculations of flooding curves, our analytical model also allows the calculation of pressure drops in countercurrent flow. Fig. 15 presents some experimental pressure drop

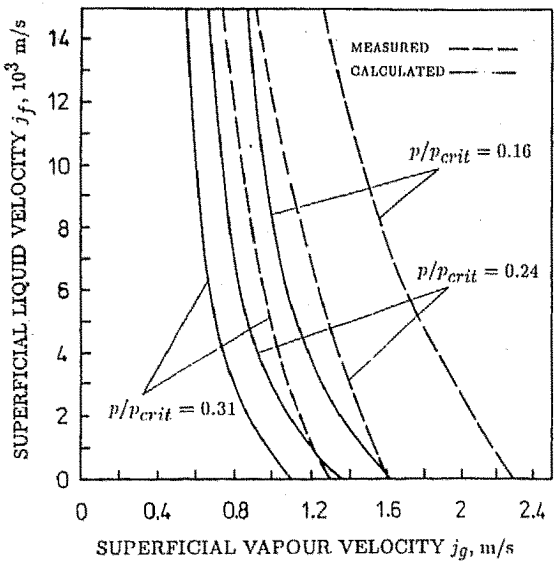

Fig. 13. Measured and empirically calculated flooding curves (conditions of present R 12 tests. Curves calculated using Eq. (19)).

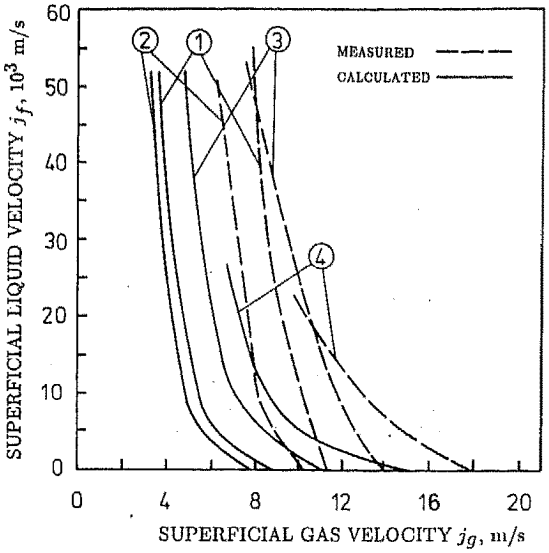

Fig. 14. Measured and empirically calculated flooding curves (conditions of low pressure reference tests 1 to 4. Curves calculated using Eq. (19)).

data in comparison with theoretical predictions from the model, for the conditions of the present Refrigerant 12 tests at p = 0.67 MPa (a) and of the air/water at atmospheric pressure experiments of Zabaras [13] (b).

The continuous lines represent the calculated Δp-curves for two different total liquid injection rates j_l^{in}. For operating points in the "stable" region left of the flooding curves, the two increasing branches of the calculated curves correspond to selected values of j_l^{in}, subsequently merging into a joint falling pressure-drop line for partial liquid delivery (flooding) conditions. The experimental data corresponding to the same values of j_l^{in} are represented by different symbols.

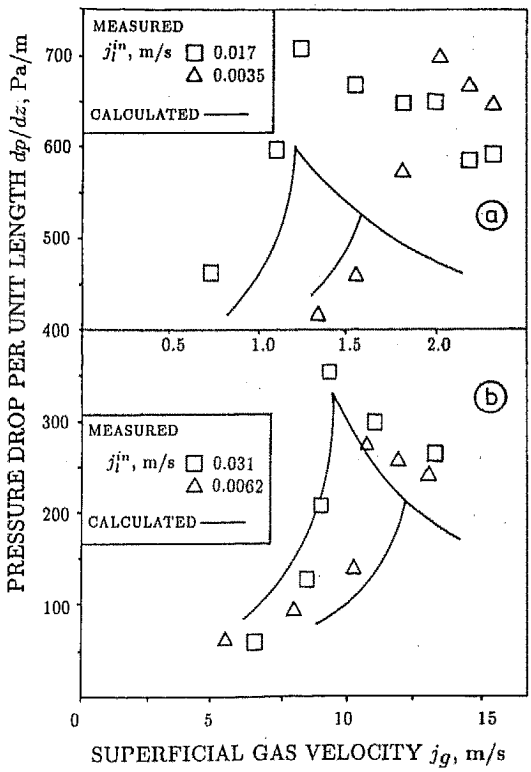

Fig. 15. Measured and analytically calculated pressure drop in countercurrent flow region (a: conditions of present R 12 tests at p = 0.67 MPa, b: conditions of air/water tests of Zabaras [13]; f_i according to Eq. (18)).

The data of Zabaras [13] are acceptably predicted in the calculations whereas, for the refrigerant test conditions, the calculated Δp-values during flooding are significantly too low. This is related to the assumption of zero core liquid fraction ($\varrho_c = \varrho_g$) in the calculations. For the air/water experiments of Zabaras [13], this simplification may be close to reality, since the high surface tension of water compared to that of Refrigerant 12 is likely to suppress liquid entrainment, thus resulting in lower core liquid fractions than in the refrigerant tests [24]. For the Refrigerant 12 test conditions at p = 0.67 MPa, the difference between calculated and measured pressure drops during flooding corresponds, according to Eq. (16), to a core liquid fraction ($1 - \bar{\varepsilon}_c$) of the order of 1%, which is in acceptable agreement with the experimental liquid fractions shown in Fig. 7.

In view of the complexity of the considered flow phenomena, the overall agreement between measured and theoretically predicted pressure drops seems very reasonable, thus further supporting the validity of the analytical flooding model proposed in this study.

Acknowledgement

The authors gratefully acknowledge financial support provided by the Bundesminister für Forschung und Technologie (BMFT).

Received: October 25, 1990 [CET 334]

Symbols used

A	[–]	dimensionless constant, Eq. (20)
B	[–]	dimensionless constant, Eq. (21)
D	[m]	diameter
f_i	[–]	interfacial friction factor
g	[m/s^2]	gravitational acceleration
j	[m/s]	superficial velocity
K	[–]	Kutateladze number
N	[–]	dimensionless constant, Eq. (18)
p	[Pa]	pressure
P	[m]	perimeter
r	[m]	radial coordinate
Re	[–]	Reynolds number
t	[s]	time
u	[m/s]	velocity
$\dot{V}$	[m^3/s]	volumetric flow rate
y	[m]	horizontal coordinate (y = 0 at the wall)
z	[m]	vertical coordinate

Greek symbols

δ	[m]	film thickness
ε	[–]	void fraction
η	[kg/ms]	viscosity
λ	[m]	wavelength
ν	[m^2/s]	kinematic viscosity
ϱ	[kg/m^3]	density
σ	[N/m]	surface tension
τ	[N/m^2]	shear stress

Indices

atm	atmospheric
c	core
calc	calculated
crit	critical
g	gas,vapour
i	interfacial
i	i = 1 or i = g
i	i = 1, 2, 3 ....
in	injected
l	liquid
meas	measured

References

[1] Bankoff, S.G., Lee, S.C., *NUREG Report CR-9060,* 1983.
[2] Tien, C.L., Liu, C.P., *EPRI Report NP-984,* 1979.
[3] Wallis, G.B., *One-Dimensional Two-Phase Flow,* McGraw-Hill, New York 1969.
[4] Pushkina, O.L., Sorokin, Y.L., *Heat Transfer – Sov. Res. 1* (1969) pp. 56 – 64.
[5] Feind, K., *VDI-Forschungsh. 481* (1960).
[6] Alekseev, V.P., Poberezkin, A.E., Gerasimov, P.V., *Heat Transfer – Sov. Res. 4* (1972) No. 6, pp. 159 – 163.
[7] McQuillan, K.W., Whalley, P.B., *Chem. Eng Sci. 40* (1985) pp. 1425 – 1440.
[8] Stephan, M., *Thesis,* TU München 1990.
[9] Auracher, H., Marroquin, A., *Proc. of 10th Brazilian Congress of Mechanical Engineering,* Rio de Janeiro 1989.
[10] Kröning, H., *Thesis,* Univ. Hannover 1984.
[11] Celata, G.P., Cumo, M., Farello, G.E., Setaro, T., *ENEA Report RT/TERM/88/3* 1988.
[12] Zabaras, G.J., Dukler, A.E., *AIChE J. 34* (1988) pp. 389 – 396.
[13] Zabaras, G.J., *Thesis,* Univ. Houston/Texas 1985.
[14] Hewitt, G.F., Lacey, P.M.C., Nicholls, B., *UKAEA Report AERE-R 4614* 1965.
[15] McQuillan, K.W., Whalley, P.B., Hewitt, G.F., *Int. J. Multiphase Flow 11* (1985) pp. 741 – 760.
[16] Suzuki, S., Ueda, T., *Int. J. Multiphase Flow 3* (1977) pp. 517 – 532.
[17] Biage, M., *Thesis,* Institut National Polytechnique de Grenoble 1989.
[18] Emmerechts, D., Giot, M., *Unpublished Work, European Two-Phase Flow Group Meeting,* Brussels, Paper E4 1988.
[19] Hewitt, G.F., *Measurement of Void Fraction,* in: *Handbook of Multiphase Systems* (G. Hetsroni, Ed.), Mc Graw-Hill/Hemisphere, New York 1982, pp. 10 – 21 – 10 – 33.
[20] Azzopardi, B.J., Teixeira, J.C.F., Jepson, D.M., *Proc. of Int. Conf. on Mechanics of Two-Phase Flows, Taipeh/R.O.C.* 1989, pp. 261 – 266.
[21] Lopes, J.C.B., *Thesis,* Univ. Houston/Texas 1984.
[22] Shearer, C.J., Davidson, J.F., *J. Fluid Mech. 22* (1965) pp. 321 – 336.
[23] Cetinbudaklar, A.G., Jameson, G.J., *Chem. Eng Sci. 24* (1969) pp. 1669 – 1680.
[24] Popov, N.K., Rohatgi, U.S., *NUREG Report CR-4630,* 1986.
[25] Clift, R., Pritchard, C.L., Nedderman, R.M., *Chem. Eng Sci. 21* (1966) pp. 87 – 95.
[26] Moalem Maron, D., Brauner, N., *Int. Comm. Heat Mass Transfer 14* (1987) pp. 45 – 55.
[27] Barnea, D., Taitel, Y., *Int. Comm. Heat Mass Transfer 12* (1985) pp. 611 – 621.
[28] Barathan, D., Wallis, G.B., Richter, H.J., *EPRI Report NP-1165,* 1979.